

Effect of droplet deformability on shear thinning in a cylindrical channel

Daniilo P. F. Silva ^{*}, Rodrigo C. V. Coelho , Margarida M. Telo da Gama , and Nuno A. M. Araújo 
Centro de Física Teórica e Computacional, Faculdade de Ciências, Universidade de Lisboa, 1749-016 Lisboa, Portugal
and Departamento de Física, Faculdade de Ciências, Universidade de Lisboa, 1749-016 Lisboa, Portugal

 (Received 10 August 2022; revised 20 December 2022; accepted 28 February 2023; published 21 March 2023)

Droplets suspended in fluids flowing through microchannels are often encountered in different contexts and scales, from oil extraction down to microfluidics. They are usually flexible and deform as a product of the interplay between flexibility, hydrodynamics, and interaction with confining walls. Deformability adds distinct characteristics to the nature of the flow of these droplets. We simulate deformable droplets suspended in a fluid at a high volume fraction flowing through a cylindrical wetting channel. We find a discontinuous shear thinning transition, which depends on the droplet deformability. The capillary number is the main dimensionless parameter that controls the transition. Previous results have focused on two-dimensional configurations. Here we show that, in three dimensions, even the velocity profile is different. To perform this study, we improve and extend to three dimensions a multicomponent lattice Boltzmann method which prevents the coalescence between the droplets.

DOI: [10.1103/PhysRevE.107.035106](https://doi.org/10.1103/PhysRevE.107.035106)

I. INTRODUCTION

Particles and droplets suspended in fluids flowing through channels are often encountered in industrial and natural processes. The flow of suspensions, microfluidic devices, and drug delivery are typical applications [1]. For instance, microfluidics has matured and provided new techniques for the control of soft suspensions. For example, this has allowed researchers to simulate microgeometries with enhanced control of droplets for a variety of applications such as the creation of emulsions and enhancement of mixing reagents, among others [2].

Generally, these complex suspensions consist of soft deformable particles which exhibit different flow behavior when compared to their hard counterparts [3,4]. Systems where particles deform due to hydrodynamic interactions have not been systematically studied, especially in three dimensions, and a deeper understanding of the key physical mechanisms underlying their single and collective behavior is needed.

There has been a growing effort to model the role of deformability in the dynamics of soft suspensions in channels. Several numerical methods have been developed. A well-known method is the boundary integral method (BIM) and its variants, especially used in the study of multiphase problems [5]. A major challenge to the use of these methods is how to accurately and effectively include surface tension. However, the BIM is applicable to certain types of flows such as Stokes or potential flows. A popular variant of the BIM is the method of interfacial dynamics [6], which is suitable for the simulation of incompressible soft particles. Using this method, it has been shown that ordered droplets driven by a pressure difference in a periodic channel accumulate at different regions of the channel depending on the viscosity

ratio between the droplet and the surrounding (continuous) fluid [7]. When the viscosity ratio is equal to unity, droplets accumulate at the center of the channel, while for higher values of the viscosity ratio the droplets may accumulate at the walls, leaving a droplet depleted zone in the middle. A more detailed study on particle migration and concentration was conducted using Stokesian dynamics in three dimensions [8], which allows accessing much smaller Reynolds numbers ($Re \ll 1$). However, it appears to be restricted in terms of applications since it is mainly limited to the study of spherical particles in Stokes flow.

The lattice Boltzmann method (LBM) provides a way to include surface tension. The LBM is commonly used to study deformable particles under different conditions [9–12]. For instance, it has been used to investigate how three-dimensional (3D) particle migration and distribution are affected by deformability and inertia at different Reynolds numbers, in particular how distinct flow focusing emerges at increasing Reynolds number for strongly deformable particles [13]. In those limits, a nonmonotonic behavior of the apparent viscosity of the suspension was reported. The LBM is an efficient algorithm allowing for extreme simulations such as with billions of grid points [14].

The flow of suspensions exhibits a wide variety of non-Newtonian behavior such as shear thinning, which has been observed in experimental studies of hard suspensions such as glass balls in oil [15] and cornstarch particles in water [16]. A striking phenomenon is the observation of shear thinning in noncolloidal suspensions reported in numerous experiments [17–20]. In these experiments, particles larger than 20 μm were used and the effects of particle migration, sedimentation, and confinement were investigated where Brownian effects are negligible [21].

Previous experimental studies have shown that shear thinning in soft suspensions of droplets depends strongly on the size of the droplets [22–24]. These experiments typically

^{*}dpsilva@fc.ul.pt

involve oil droplets in water studied over a large range of volume fractions. In parallel with experiments, shear thinning has also been reported in emulsions through numerical simulations, for example, using interface tracking methods [25]. The collective dynamics of a large number of deformable particles in microchannels was also investigated [26] via 3D simulations using an immersed boundary method. Additionally, the immersed boundary method has been used to address more complex situations such as the implementation of membrane viscosity in fluid-filled bodies like capsules [27,28]. The trajectories and the plug-flow profile of the particles were analyzed as a function of the deformability and channel size.

Other works [29,30] investigated the effect of elasticity and confinement of capsules such as red blood cell suspensions for different cell rigidity. They observed shear thinning behavior and reported that at high enough capillary numbers the effective viscosity of the suspension converges to the solvent viscosity. These studies suggest that a key parameter when investigating the flow of deformable particles is the capillary number, defined as the ratio of viscous forces to interfacial tension forces.

Recently, a discontinuous shear thinning behavior was reported in the flow of deformable droplets in two dimensions [31,32]. This behavior is associated with a nonequilibrium transition between a soft and a hard phase, which depends on the area fraction of droplets in suspension and the applied pressure difference. Strong shear thinning behavior was reported at a higher area fraction and it was further revealed that when the area fraction is higher than 0.5, the shear thinning becomes discontinuous, i.e., there is a jump in the viscosity at a critical value of the forcing. In addition, the velocity (in the flow direction) was measured and it was reported that the velocity of the droplets remains close to that of the continuous fluid throughout the channel. Simulations were performed using a 2D hybrid LBM. A more recent study [33] investigated and confirmed the robustness of this discontinuous behavior. This study reported additional discontinuous jumps in viscosity over a larger parameter range, showing how the discontinuous shear thinning is preserved at lower values of the confinement, defined as the ratio between channel height and droplet radius. To do so, they simulated a large 2D system with up to 500 droplets (approximately 0.85 of the area fraction).

The effect of the viscosity ratio as well as the ratio of droplet to channel radius was also investigated. While discontinuous shear thinning behavior of droplets has been investigated over a wide parameter range in two dimensions, these effects have not yet been identified and tested in 3D geometries. In particular, it is elusive how deformability affects the discontinuous shear thinning and the overall fluid flow in 3D systems. In this paper we simulate droplets in 3D flows and investigate the discontinuous shear thinning behavior as a function of the surface tension, which is related to droplet deformability. We improve and extend to three dimensions a multicomponent LBM with frustrated coalescence [34]. We analyze the shear thinning for different flow conditions and droplet deformability and discuss the main properties of the velocity profiles.

The paper is organized as follows. The lattice Boltzmann model is described in Sec. II. In Sec. III the effect of droplet

TABLE I. Velocity vectors and weights for the D3Q41 lattice. The speed of sound c_s^2 is $1 - \sqrt{2/5}$.

| \mathbf{c}_i | w_i |
|---|--------------------------------|
| (0,0,0) | $2(5045 - 1507\sqrt{10})/2025$ |
| ($\pm 1, 0, 0$), ($0, \pm 1, 0$), ($0, 0, \pm 1$) | $377/(5\sqrt{10}) - (91/40)$ |
| ($\pm 1, \pm 1, 0$), ($\pm 1, 0, \pm 1$), ($0, \pm 1, \pm 1$) | $(55 - 17\sqrt{10})/50$ |
| ($\pm 1, \pm 1, \pm 1$) | $(233\sqrt{10} - 730)/1600$ |
| ($\pm 3, 0, 0$), ($0, \pm 3, 0$), ($0, 0, \pm 3$) | $(295 - 92\sqrt{10})/16200$ |
| ($\pm 3, \pm 3, \pm 3$) | $(130 - 41\sqrt{10})/129600$ |

deformability is studied for a dense suspension flow in a 3D cylindrical channel. We highlight the differences and similarities between the results in 2D and 3D flows. In Sec. IV we make some final observations. The Appendix contains numerical validation [35].

II. METHOD

We extended to three dimensions a multicomponent model with frustrated coalescence. For flexible droplets, the motion of the fluid is represented by a set of distribution functions $f_{k,i}(\mathbf{x}, t)$ at position \mathbf{x} and time t , where the subscripts k and i denote the fluid component and discrete velocity directions, respectively. The time evolution of $f_{k,i}(\mathbf{x}, t)$ is given by the discrete Boltzmann equation

$$f_{k,i}(\mathbf{x} + \mathbf{c}_i, t + 1) - f_{k,i}(\mathbf{x}, t) = -\frac{1}{\tau_k} [f_{k,i}(\mathbf{x}, t) - f_{k,i}^{eq}(\mathbf{x}, t)] + \mathcal{F}_{k,i}, \quad (1)$$

where τ_k is the relaxation time for each component and $\mathcal{F}_{k,i}$ is the forcing term. Unless otherwise stated, we express our results in lattice units (l.u.), which means that the lattice spacing Δx and the time step Δt are equal to one. The equilibrium distribution is given by

$$f_{k,i}^{eq} = \rho_k w_i \left[1 + \frac{\mathbf{u}^{eq} \cdot \mathbf{c}_i}{c_s^2} + \frac{(\mathbf{u}^{eq} \cdot \mathbf{c}_i)^2}{2c_s^4} - \frac{(\mathbf{u}^{eq})^2}{2c_s^2} \right], \quad (2)$$

where c_s is the speed of sound. The lattice used in the streaming step is the D3Q41 lattice (see Table I for the vectors \mathbf{c}_i and weights w_i). As will be discussed, using higher-order lattices to solve the Boltzmann equation reduces the spurious velocities. Here \mathbf{u}^{eq} is the equilibrium velocity given by

$$\mathbf{u}^{eq} = \frac{\sum_k \frac{\rho_k \mathbf{u}_k}{\tau_k}}{\sum_k \frac{\rho_k}{\tau_k}}, \quad (3)$$

where $\rho_k \mathbf{u}_k$ is the k th component of momentum. The Guo forcing scheme [36] was adopted to implement the forces acting in a fluid as it yields a viscosity-independent surface tension. Thus,

$$\mathcal{F}_{k,i} = \left(1 - \frac{1}{2\tau_k} \right) w_i \left[\frac{\mathbf{c}_i - \mathbf{u}^{eq}}{c_s^2} + \frac{(\mathbf{c}_i \cdot \mathbf{u}^{eq}) \mathbf{c}_i}{c_s^4} \right] \cdot \mathbf{F}_k, \quad (4)$$

TABLE II. Velocity vectors and weights for the D3Q39 lattice. The speed of sound c_s^2 is $2/3$.

| \mathbf{c}_i | w_i |
|---------------------------|--------|
| (0,0,0) | 1/12 |
| ($\pm 1, 0, 0$) | 1/12 |
| ($\pm 1, \pm 1, \pm 1$) | 1/27 |
| ($\pm 2, 0, 0$) | 2/135 |
| ($\pm 2, \pm 2, 0$) | 1/142 |
| ($\pm 3, 0, 0$) | 1/1620 |

where \mathbf{F}_k is the sum of all the forces. The equilibrium velocity is the same as in Eq. (2) [36]. Also,

$$\rho_k = \sum_{i=0}^{40} f_{k,i}, \quad \rho_k \mathbf{u}_k = \sum_{i=0}^{40} f_{k,i} \mathbf{c}_i + \frac{\mathbf{F}_k}{2}. \quad (5)$$

The barycentric velocity \mathbf{u} of the fluid mixture, i.e., the physical velocity, is given by

$$\mathbf{u} = \frac{\sum_k \rho_k \mathbf{u}_k}{\rho}, \quad \rho = \sum_k \rho_k, \quad (6)$$

where ρ is the total density of the fluid mixture.

There are three internal forces acting on the fluid: an intracomponent short-range attractive force, a midrange repulsive force, and a repulsive force between different components. The midrange force prevents droplet coalescence and for that we use the D3Q39 lattice [37] (see Table II). For the attractive short-range and repulsive forces between components, we use the D3Q41 lattice [37]. The intracomponent forces acting on the same component are

$$\begin{aligned} \mathbf{F}_k^c = & -G_{k,1} \psi_k(\mathbf{x}) \sum_{i=0}^{40} w_i \psi_k(\mathbf{x} + \mathbf{c}_i) \mathbf{c}_i \\ & - G_{k,2} \psi_k(\mathbf{x}) \sum_{j=0}^{38} p_j \psi_k(\mathbf{x} + \mathbf{c}_j) \mathbf{c}_j, \end{aligned} \quad (7)$$

where $\psi_k(\rho_k) = \rho_0(1 - e^{-\rho_k/\rho_0})$ is a pseudopotential with a uniform reference density ρ_0 . Additionally, $G_{k,1}$ and $G_{k,2}$ are the self-interaction forces within each component. The repulsive forces between the components are implemented as usual [38]:

$$\mathbf{F}_k^r = -\rho_k(\mathbf{x}) \sum_{\bar{k}} G_{\bar{k}k} \sum_{i=0}^{40} w_i \rho_{\bar{k}}(\mathbf{x} + \mathbf{c}_i) \mathbf{c}_i. \quad (8)$$

The adhesion force with the solid boundary is given by

$$\mathbf{F}_k^s = -G_{ks} \rho_k(\mathbf{x}) \sum_{i=0}^{\text{solid}} w_i s(\mathbf{x} + \mathbf{c}_i) \mathbf{c}_i, \quad (9)$$

where $s(\mathbf{x})$ is the switch function, which takes the values 0 and 1 for fluid and solid nodes, respectively, and G_{ks} is the interaction strength between fluid component k and the solid boundary. The subscript k represents the component A or B . Additionally, to the force (9), other forces [Eqs. (8) and (7)] are applied to the solid nodes by using a virtual solid density, which in our case is the initial density of the surrounding

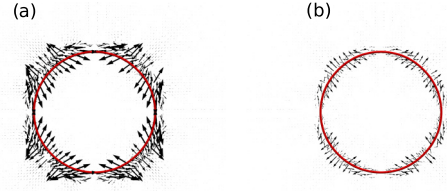


FIG. 1. Spurious velocities (arrows) around a circular interface (red) of radius $r = 20$ at equilibrium for $G_{k,1} = -7.9$ and $G_{k,2} = 4.9$. The largest spurious velocities are (a) 0.017 l.u. for the D3Q19 lattice and (b) 0.0092 l.u. for the D3Q41 lattice. The velocity field is on the same scale in both panels. The ratio of the density inside and outside the droplet is 1.133 for D3Q19 and 1.062 for D3Q41.

fluid. We use $G_{ks} = -0.35$, resulting in a contact angle of 90° (neutral wetting).

The total force \mathbf{F}_k in Eq. (4) is the sum of the external body forces \mathbf{F}_k^b (e.g., gravity, which we neglect here), the internal forces, and the solid boundary interaction force: $\mathbf{F}_k = \mathbf{F}_k^b + \mathbf{F}_k^c + \mathbf{F}_k^r + \mathbf{F}_k^s$. For simplicity, we assume that $G_{A,1} = G_{B,1}$, $G_{A,2} = G_{B,2}$, and $G_{A,B} = G_{B,A}$. The parameters $G_{A,1}$, $G_{B,2}$, etc., are the strength coefficients of the interaction forces. More specifically, a positive (or negative) strength coefficient represents a repulsive (or attractive) interaction. To have the desired repulsive and attractive forces $G_{k,1} < 0$, $G_{k,2} > 0$, and $G_{k,\bar{k}} > 0$. In the competing force \mathbf{F}_k^c , the attractive force must overcome the repulsive force to form droplets, so we set $|G_{k,1}| > |G_{k,2}|$. Details on how the strength parameters $G_{k,1}$, $G_{k,2}$, and $G_{k,\bar{k}}$ and reference density ρ_0 are related to the surface tension can be found in [39].

Multiphase and multicomponent LBMs suffer from spurious velocities caused by an imbalance between the interaction forces. These velocities can increase if the viscosity ratio deviates much from one or if the surface tension is high. Thus, the simulations might become unstable for realistic physical parameters. Previous works have demonstrated that by increasing the isotropy of the lattice used to calculate the interaction forces in the pseudopotential models it is possible to reduce the spurious velocities [40–42]. In two dimensions the lattice used for the midrange repulsive force was D2Q25 [43,44]. In three dimensions the equivalent of the D2Q25 lattice would be a D3Q125 lattice, which includes all the neighbors in the first and second belts. However, such a lattice would be computationally expensive. Instead, we use the D3Q39 lattice for the midrange force (see Tables I and II). A nonphysical effect causes droplets to become glued in the direction of the diagonal vectors of the lattice. We also observe this effect in the usual 2D models [39,41,45]. Peng *et al.* [46] showed that using lattices with higher isotropy in the streaming process significantly reduces the spurious velocities. In our simulations, we use an eighth-order isotropic lattice in the streaming step. By contrast, the D3Q19 lattice has only fourth-order isotropy. In Fig. 1 we compare the spurious velocities when these two lattices are used in the streaming step. We note that it reduces spurious velocities by nearly one-half. Notice in Fig. 1 that spurious velocities are stronger in the diagonal direction of the grid, which explains why the droplets stick to each other at these points but not along the grid axes.

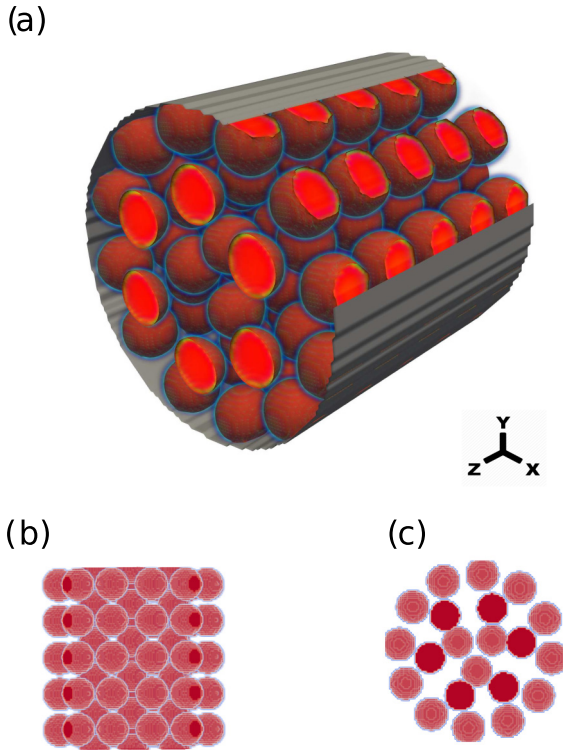


FIG. 2. Initial setup. (a) Here 105 droplets are arranged in a hexagonally non-close-packed system with a volume fraction of 0.61. A force \mathbf{F} is imposed in the z direction and varied. The walls have a neutral wetting condition [47]. The droplets (red) are inside the cylindrical channel (gray). The system is periodic in the direction of the flow. The parameters for the interactions are $G_{k,1} = -7.9$ and $G_{k,2} = 4.9$ and the viscosity ratio of the droplet and the continuous fluid is set to one. (b) Top view. (c) Front view.

Regarding computational cost, in the present model the number of droplets does not increase the computational cost at a given system size. This is because the repulsion between droplets is based on the density of each lattice Boltzmann node. In other models [27,28], an increase in the number of immersed flexible fluid-filled bodies leads to an increase in computation, which is significant for a larger number of immersed objects. However, these do not suffer from spurious velocities as in the present model. They describe fundamentally different mechanisms due to the different boundary conditions on the droplet and the capsule. While the capsule has a fluid-solid boundary, the droplet has a fluid-fluid boundary.

III. FLOW OF DROPLETS

To understand the effect of droplet deformability on the overall flow of concentrated suspensions, we simulate a densely packed system of 105 droplets of radius $r = 8$ lattice units in a 3D cylindrical channel with periodic boundary conditions in the z direction (see Fig. 2). The droplets are not close packed, resulting in a total volume fraction of 0.61. Initially, the droplets cannot be close packed; otherwise they

will coalesce immediately due to the presence of diffusive interfaces. Thus, we allow a small distance between the droplets (three to five lattice points) to avoid this. So, while not fully jammed, the droplets are in close contact with each other. Our simulations are parallelized using OPENMP and we use eight cores for our simulations, each with 2.3 GHz. Our simulations deliver approximately 1.8×10^6 lattice updates per second. The length and radius of the cylinder are 95 and 47.5 l.u., respectively. We impose no-slip boundary conditions in velocity and a neutral wetting boundary condition which creates a layer of wetting droplets along the wall. The fluid is driven by a fixed external force. Figure 2 shows a snapshot of the initial setup.

To study the effect of droplet deformability we first vary the external force \mathbf{F} in the z direction and measure the effective relative viscosity $\mu_r = \mu/\mu_0$, where μ is the (apparent) dynamic viscosity of the fluid with droplets and μ_0 is the dynamic viscosity of the fluid without droplets. The effective viscosity in terms of the volume flow rate

$$\mu_r = \frac{Q_0}{Q} \quad (10)$$

is measured, where Q_0 is the flow rate of the fluid without droplets and Q is the flow rate with droplets. The flow rate Q is defined as $Q = \int_A v_z dA$, where v_z is the axial velocity and A is the cross-sectional area. This measurement of μ_r is obtained for different values of surface tension γ (by varying ρ_0). The surface tension may be used as a measure of the droplet deformability; however, since we compare forces resulting from fluid motion with forces resulting from surface tension, the capillary number $Ca = \mu_0 v / \gamma$ is a more appropriate dimensionless parameter, where v is the characteristic velocity (taken as the maximum velocity of the fluid). We vary it by changing the surface tension. The flow rate is measured along a plane perpendicular to the flow (XY). We measure the flow velocity on each lattice node along this plane to obtain the overall flow rate Q at a particular time step. Due to the discretization of the droplets on the lattice, the value of Q fluctuates around an average value, as the intersection of the flowing droplets with the plane is not fixed. Then Q is averaged over subsequent instants of time (over 15 frames with 5000 iterations between them) in the steady state. We study the relationship between effective viscosity and surface tension. We plot the dependence of μ_r on the surface tension in Fig. 3. In Fig. 3 we see the discontinuous behavior which happens at larger values of \mathbf{F} as we increase the surface tension. In addition, we see that the viscosity curves collapse when plotted against the capillary number. The discontinuous drop of the viscosity suggests shear thinning. For soft particles, deformability has been shown to promote shear thinning analogous to cells flowing in microenvironments [48]. We report data collapse in both regimes by taking the maximal velocity in each respective regime (before or after shear thinning) as shown in Fig. 3(b). Shear thinning is also observed in non-Brownian hard-sphere suspensions [49] and the decrease in viscosity has been studied under more controlled conditions for those particles [17,50]. The results are nearly independent of the size of the channel [35]. For a channel with 170 nodes, the largest difference between the two curves of relative viscosity is less

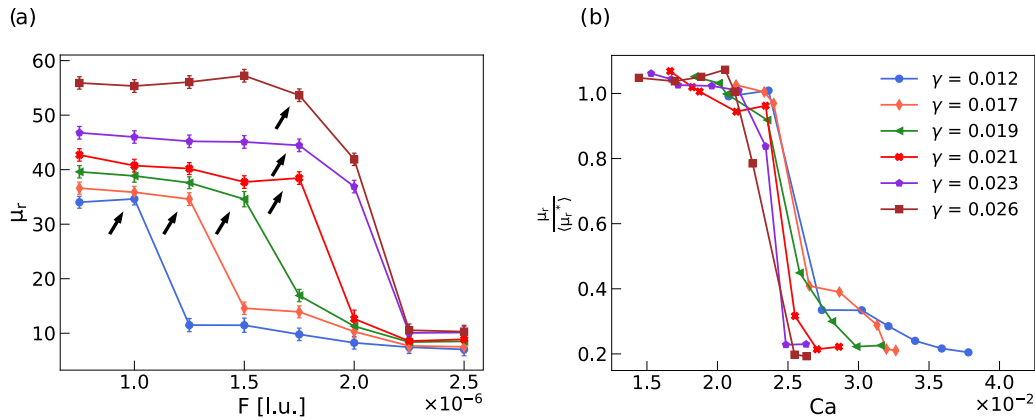


FIG. 3. Discontinuous shear thinning for different values of γ . (a) Discontinuous shear thinning occurs for progressively larger values of the external force which drives the flow. The black arrow indicates the threshold viscosity μ_r^* , i.e., the relative viscosity before shear thinning. (b) Relative viscosity μ_r (normalized by the threshold viscosity μ_r^*) as a function of the capillary number Ca . The transition is at approximately 0.025. Simulations were carried out for different values of surface tension γ .

than 2%. This information can be found in the Supplemental Material [35], which includes Refs. [51,52].

We define F^* as the threshold force applied to the system necessary to trigger discontinuous shear thinning (see Fig. 4). We observe that at higher values of γ the force required to trigger discontinuous shear thinning F^* increases in a roughly linear fashion until it saturates. This is shown in Fig. 4(a). In fact, as we increase γ the droplets become less flexible and eventually reach a state similar to that of hard particles. We expect in that limit shear thickening, as reported, for example, in Ref. [15] for hard suspensions (cornstarch in water and glass spheres in oil) between parallel plates (rotating top plate). Figure 4(b) shows that as the droplets become less deformable (increasing γ), the threshold viscosity μ_r^* increases.

The simulations are performed for a fixed value of the ratio between the channel diameter and the droplet radius. In two dimensions [33], it is reported that the effective relative viscosity μ_r increases with this ratio. We do not vary this ratio, but we do not expect that the effect of confinement is qualitatively different in three dimensions. The fully developed velocity profile across a cylindrical channel with no droplets can be computed analytically from the Navier-Stokes equations. For a cylindrical channel with a circular cross section of radius R , the solution is a parabolic velocity distribution [53]. The velocity distribution for droplets suspended

in flow is however more complex. The flow in this channel is described by small characteristic dimensions and velocities. Consequently, the flow is characterized by low Reynolds number Re and is laminar. Low- Re flows also indicate that the viscous forces are relevant. While the flow is laminar, the regime is not Stokesian. Viscous forces usually arise due to friction, for example, near the walls. The presence of both suspended and adhered droplets in a 3D channel leads to distinct profiles. In particular, the droplets adhered at the channel wall offer resistance to the flow of other droplets up to a certain point.

We plot the velocity distribution as a function of the nondimensional radius r/R . We measure the velocities of the continuous phase and of the droplet phase separately before (high μ_r) and after (low μ_r) the discontinuous shear thinning. An average in space is taken between the radial distances r and $r + \Delta r$, at a fixed Δr in steady-state flow. The velocities of the droplet phase $v_d(r)$ and of the continuous phase $v_f(r)$ are identified by means of the density field for the droplet component. A threshold of 0.6 is considered, which is half of the density of the droplets, 1.2. Regions with density above this threshold are considered part of the droplets, while those below are part of the continuous fluid. The diffusive interface has a thickness of 2.84 l.u. The Δr value is 6 l.u. for droplets and 4 l.u. for continuous fluid. When shear thinning has occurred, the $v_f(r)$ and $v_d(r)$ are similar and are consistent with plug flow behavior. Before shear thinning the flow is no longer well described as plug flow (as reported in two dimensions [32]), i.e., the radial profile of the continuous fluid velocity defined as $v_f(r) = \langle v_f(r, \theta, z) \rangle$ in cylindrical coordinates is higher than that of the droplets phase $v_d(r) = \langle v_d(r, \theta, z) \rangle$. The average is taken along z and angle θ . After shear thinning $v_f(r) \approx v_d(r)$. We also observe that for a low number of droplets, no shear thinning occurs (plot not shown) as in two dimensions. The situation before shear thinning, however, contrasts with that of a 2D channel where the system flows slowly and is in a nearly jammed state. While previous studies in two dimensions [31,33] have not reported differences between the fluid and droplet velocity before shear thinning, we observe differences in a 3D

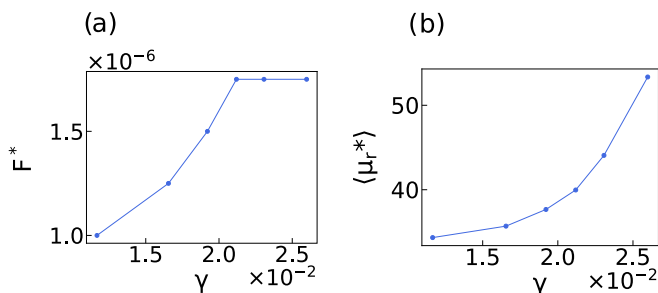


FIG. 4. (a) Threshold force F^* required to trigger discontinuous shear thinning as a function of γ . Here F^* increases roughly linearly with the droplets' surface tension. (b) Corresponding threshold viscosity μ_r^* as a function of γ .

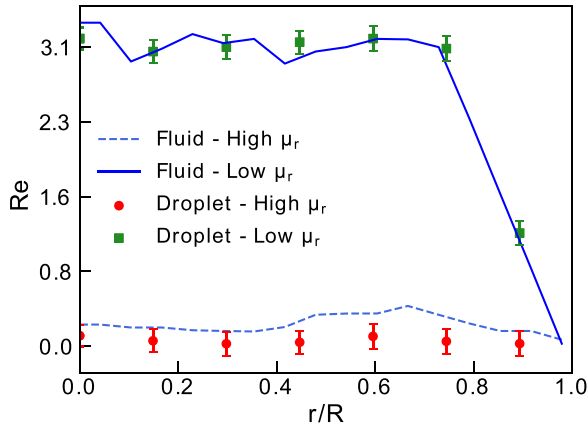


FIG. 5. Velocity profile given by the dimensionless Reynolds number $Re = \frac{\langle V_z \rangle D}{\nu}$, where D is the diameter of the channel, ν is the kinematic viscosity, and $\langle V_z \rangle$ is the average velocity in the z direction. The capillary numbers are $Ca = 0.017$ and 0.0314 . The droplet and fluid velocity are plotted separately.

geometry. The velocity of the continuous fluid $v_f(r)$ is significantly higher than $v_d(r)$, as shown in Fig. 5. We point out that for a 3D channel there is space between the droplets (see Fig. 6) for the continuous fluid to flow in contrast to the 2D case with a similar arrangement. While the velocity is continuous at the interface, the gaps between some droplets are large enough [see Fig. 2(c)] so that before shear thinning the average continuous fluid flows $\langle v_f(r) \rangle$ with a higher velocity than the average velocity of the droplets phase $\langle v_d(r) \rangle$. In Fig. 5, before shear thinning $\langle v_f(r) \rangle$ and $\langle v_d(r) \rangle$ are 0.00088 and 0.00021 , respectively. Thus, the continuous fluid flows 4.2 times faster than the droplets for this particular force.

As we increase the forcing, the fluid eventually pushes the droplets, leading to the discontinuous shear thinning. The droplets and fluid then flow with matching velocities. We highlight that, although simulations in 2D geometries can capture the essential flow qualities such as discontinuous shear thinning and plug flow behavior, 3D geometries give more realistic results (in two dimensions a circular cross section would be representing a cylinder and not a sphere like

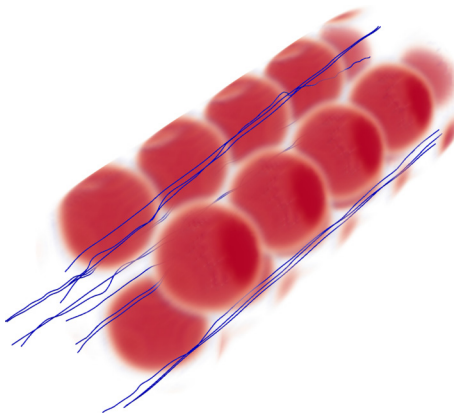


FIG. 6. Streamlines (blue) for a central region of the channel just before shear thinning, which indicates that the continuous fluid flows between droplets (red). The system has $Ca = 0.025$.

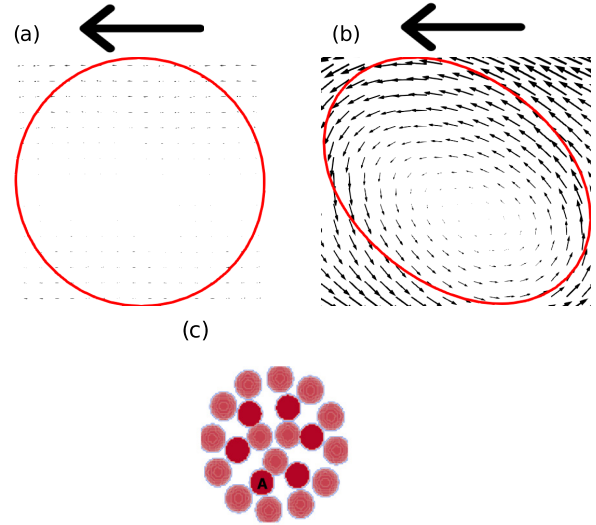


FIG. 7. Relative velocity fields and droplet shape cross section (a) before and (b) after discontinuous shear thinning. The capillary numbers are (a) $Ca = 0.017$ and (b) $Ca = 0.0314$. The relative velocity is obtained by subtracting the velocity at the center of the droplet and it is on the same scale in both images. The cross section is obtained along the ZY plane. Large black arrows indicate the direction of flow. (c) Relative position of the sample droplet in question marked as A (front view, i.e., XY plane).

in the case of a droplet), in particular, the difference between the droplet and continuous fluid velocities. The flow of the continuous fluid between 2D droplets is affected by geometrical restrictions caused by narrow passages and dead-end pores between droplets [54,55], especially at high area fractions. By contrast, 3D geometries with droplets allow significant interconnected space between the droplets and therefore the continuous fluid can flow through it. The importance of this effect and the role it plays in the hydrodynamics of droplets are not well understood.

The deformation of the droplets also causes distinct internal flows. Figures 7(a) and 7(b) show cross sections of a nondeformed droplet before and a deformed droplet after shear thinning, respectively. The droplet in question is next to the wetting layer of droplets. Droplet deformation is naturally associated with shear thinning as the deformation promotes the flow of droplets. In line with the results in two dimensions [31], not only do the droplets deform but internal currents are set up within the deformed droplets. Notice that the internal flow is almost nonexistent before shear thinning when the droplets are hardly deformed.

IV. CONCLUSION

We have simulated the flow of droplets in a 3D channel. For progressively higher values of the external force, we observed discontinuous shear thinning. We studied in this transition the effect of the surface tension, which is proportional to the droplet deformability. At higher surface tension the droplets are less deformable and thus larger values of force are required for discontinuous shear thinning to occur. We observed that this transition occurs at a given capillary number. We also

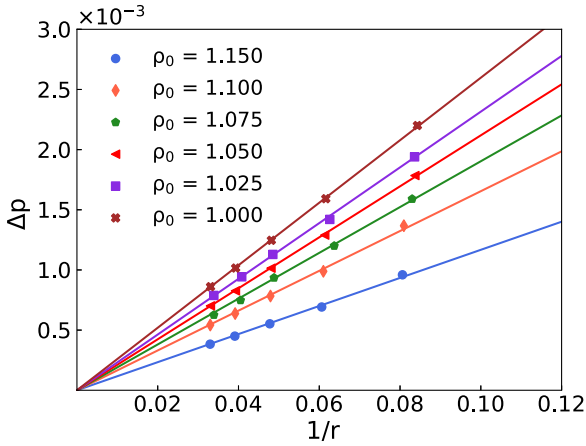


FIG. 8. Pressure difference Δp as a function of the inverse of the droplet radius r . We simulate a static droplet for a fixed ρ_0 (reference density) and let it reach the steady state. The symbols represent the pressure difference inside and outside the droplet in our simulations. The solid lines are linear fits corresponding to Eq. (A1), where the slope is γ .

noticed that μ_r increases with the surface tension. This is to be expected as the droplets become less deformable. Simulations for low volume fractions do not exhibit any discontinuous shear thinning in line with 2D studies. We analyzed the velocity profiles before and after shear thinning and noticed that after shear thinning the velocity profile is that of plug flow similar to 2D flows. However, closer inspection of the velocity profile before shear thinning revealed an essential feature that distinguishes our results from those in two dimensions. We noticed that the fluid and droplet velocities are different, with the fluid velocity being higher and that of the droplets being near zero. Additionally, we were able to observe internal currents in the droplets after shear thinning. A possible extension of this study is to analyze how the viscosity ratio (between the droplets and the fluid) affects the overall flow.

To carry out this study we extended to three dimensions a previous multicomponent LBM that prevents coalescence between the droplets. We measured the disjoining pressure, which is independent of the viscosity ratio. We were able to reduce spurious velocities which cause unphysical effects in the simulations such as sticking droplets and coalescence when a collision occurs in certain directions. This was achieved by using higher-order lattices in the streaming step.

We note some prospects for experimental studies of deformable droplets in microchannels. Recently, hydrodynamic

TABLE III. Surface tension γ for different reference densities ρ_0 in lattice units. The values of γ are obtained from linear fits in Fig. 8.

| ρ_0 | γ |
|----------|----------|
| 1.000 | 0.026 |
| 1.025 | 0.023 |
| 1.050 | 0.021 |
| 1.075 | 0.019 |
| 1.100 | 0.017 |
| 1.150 | 0.012 |

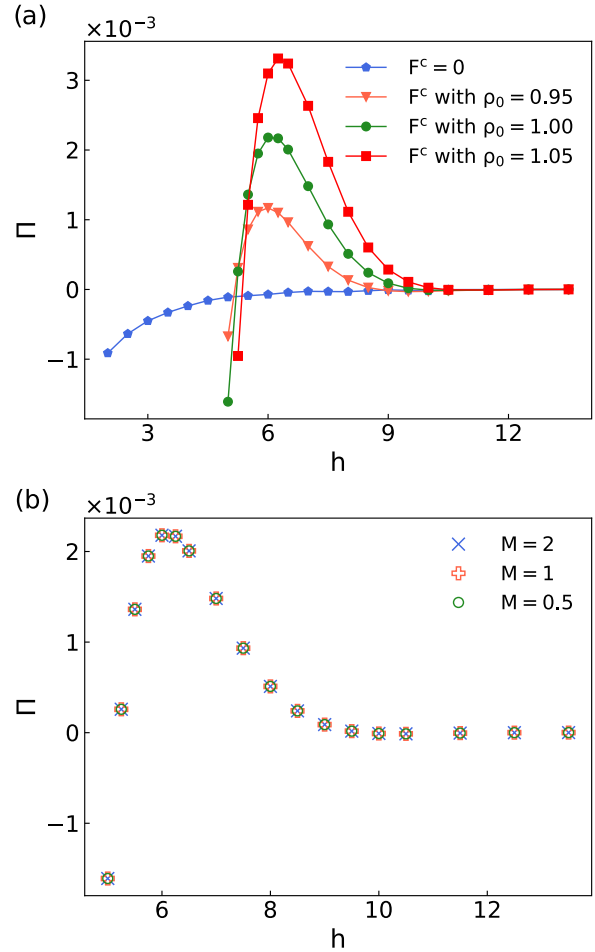


FIG. 9. Disjoining pressure Π as a function of the distance h between two flat interfaces with fixed $G_{k,1} = -3.5$ and $G_{k,2} = 2.5$ achieved with competing forces F^c given by Eq. (7), which provides the repulsive force to avoid coalescence. A positive value indicates repulsion, while a negative value indicates attraction. (a) Disjoining pressure for different values of the reference density ρ_0 . (b) Disjoining pressure for different values of the viscosity ratio M with $\rho_0 = 1.00$.

resistance (the extra resistance due to the presence of an object in a channel) has been suggested as a parameter for characterizing such flows [56]. It would be interesting to calculate the dependence of the hydrodynamic resistance on the capillary number in experiments with a setup similar to the one presented in this paper.

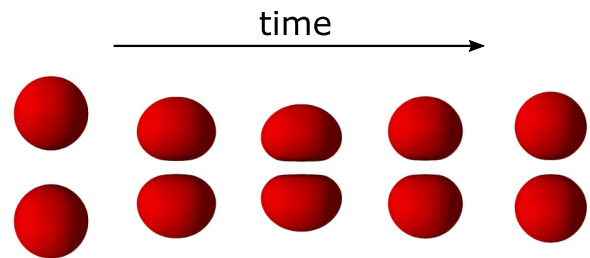


FIG. 10. Snapshots of a collision between two droplets illustrating the frustrated coalescence.

ACKNOWLEDGMENTS

We acknowledge financial support from the Portuguese Foundation for Science and Technology under Contracts No. PTDC/FIS-MAC/28146/2017 (LISBOA-01-0145-FEDER-028146), No. UIDB/00618/2020, No. UIDP/00618/2020, and No. 2020.08525.BD.

There are no conflicts of interest to declare.

APPENDIX: NUMERICAL TESTS

In this Appendix we analyze the properties of the 3D multicomponent method. We measure the surface tension, which is related to the deformability of the droplets, and we analyze the disjoining pressure. To measure the surface tension, we perform the Laplace test in two dimensions. At equilibrium, the curved interface of a static droplet increases the pressure inside the droplet. The radius, pressure difference, and surface tension must satisfy the Young-Laplace equation [38]

$$\Delta p = p_{\text{in}} - p_{\text{out}} = \frac{\gamma}{r}, \quad (\text{A1})$$

where r is the radius of the droplet, p_{in} and p_{out} are the pressures inside and outside the droplet, respectively, and γ is the surface tension. To test Laplace's law, a series of

LBM simulations with different values for the droplet radius were performed. As seen in Fig. 8, the pressure difference Δp increases linearly with the inverse of the droplet radius r (curvature). To vary the surface tension, we fix the parameters $G_{k,1}$ and $G_{k,2}$ and change the uniform reference density ρ_0 (effectively varying the interaction forces). The solid lines represent results calculated from Laplace's law and the symbols are obtained from the simulations. The slope of the solid lines is γ . The simulation results are consistent with Laplace's law. The values of γ are shown in Table III. The ratio of the total densities inside and outside the droplets for the values of $\rho_0 = 1.000$ and 1.150 are 1.058 and 1.062 , respectively. When the parameter G_{AB} exceeds a certain threshold it gives rise to stable interfaces between fluids A and B with positive surface tension. However, when the droplets approach each other, a thin film is formed, leading to coalescence. The phase separation promotes negative disjoining pressure and thus the competing interactions prevent the coalescence of neighboring droplets and give rise to positive disjoining pressure as seen in Fig. 9. This mechanism has been used in other studies to simulate noncoalescing droplets [34,57,58]. We further show this mechanism in action for 3D droplets, in Fig. 10. The disjoining pressure is also independent of the viscosity ratio M defined as the viscosity of the droplet over the viscosity of the continuous fluid [59].

-
- [1] Q. Xu, M. Hashimoto, T. T. Dang, T. Hoare, D. S. Kohane, G. M. Whitesides, R. Langer, and D. G. Anderson, *Small* **5**, 1575 (2009).
- [2] S. Sohrabi, N. Kassir, and M. K. Moraveji, *RSC Adv.* **10**, 27560 (2020).
- [3] N. Koumakis, A. Pamvouxoglou, A. S. Poulos, and G. Petekidis, *Soft Matter* **8**, 4271 (2012).
- [4] K. van der Vaart, Y. Rahmani, R. Zargar, D. Bonn, and P. Schall, *J. Rheol.* **57**, 1195 (2013).
- [5] T. Hou, J. Lowengrub, and M. Shelley, *J. Comput. Phys.* **169**, 302 (2001).
- [6] C. Pozrikidis, *J. Comput. Phys.* **169**, 250 (2001).
- [7] H. Zhou and C. Pozrikidis, *Phys. Fluids* **6**, 80 (1994).
- [8] P. R. Nott and J. F. Brady, *J. Fluid Mech.* **275**, 157 (1994).
- [9] B. Dünweg and A. J. C. Ladd, *Adv. Polym. Sci.* **221**, 89 (2009).
- [10] T. Krüger, F. Varnik, and D. Raabe, *Comput. Math. Appl.* **61**, 3485 (2011).
- [11] Y. Chen, *RSC Adv.* **4**, 17908 (2014).
- [12] R. C. V. Coelho, D. P. F. Silva, A. M. R. Maschio, M. M. T. da Gama, and N. A. M. Araújo, *Phys. Fluids* **35**, 013304 (2023).
- [13] T. Krüger, B. Kaoui, and J. Harting, *J. Fluid Mech.* **751**, 725 (2014).
- [14] G. Falcucci, G. Amati, P. Fanelli, V. K. Krastev, G. Polverino, M. Porfiri, and S. Succi, *Nature (London)* **595**, 537 (2021).
- [15] E. Brown and H. M. Jaeger, *Phys. Rev. Lett.* **103**, 086001 (2009).
- [16] A. Fall, F. Bertrand, D. Hautemayou, C. Mezière, P. Moucheront, A. Lemaître, and G. Ovarlez, *Phys. Rev. Lett.* **114**, 098301 (2015).
- [17] I. E. Zarraga, D. A. Hill, and D. T. Leighton, *J. Rheol.* **44**, 185 (2000).
- [18] S. Dai, E. Bertevas, F. Qi, and R. I. Tanner, *J. Rheol.* **57**, 493 (2013).
- [19] Y. Lin, G. W. H. Tan, N. Phan-Thien, and B. C. Khoo, *J. Non-Newtonian Fluid Mech.* **212**, 13 (2014).
- [20] A. Singh and P. R. Nott, *J. Fluid Mech.* **490**, 293 (2003).
- [21] N. A. M. Araújo, L. M. C. Janssen, T. Barois, G. Boffetta, I. Cohen, A. Corbetta, O. Dauchot, M. Dijkstra, W. M. Durham, A. Dussutour, S. Garnier, H. Gelderblom, R. Golestanian, L. Isa, G. H. Koenderink, H. Löwen, R. Metzler, M. Polin, C. P. Royall, A. Larić *et al.*, *Soft Matter* **19**, 1695 (2023).
- [22] Y. Otsubo and R. K. Prud'homme, *Rheol. Acta* **33**, 303 (1994).
- [23] R. Pal, *AIChE J.* **42**, 3181 (1996).
- [24] R. Pal, *J. Colloid Interface Sci.* **225**, 359 (2000).
- [25] M. Loewenberg and E. J. Hinch, *J. Fluid Mech.* **321**, 395 (1996).
- [26] S. K. Doddi and P. Bagchi, *Phys. Rev. E* **79**, 046318 (2009).
- [27] F. Guglietta, M. Behr, L. Biferale, G. Falcucci, and M. Sbragaglia, *Philos. Trans. R. Soc. A* **379**, 20200395 (2021).
- [28] F. Guglietta, M. Behr, L. Biferale, G. Falcucci, and M. Sbragaglia, *Soft Matter* **16**, 6191 (2020).
- [29] G. R. Lázaro, A. Hernández-Machado, and I. Pagonabarraga, *Soft Matter* **10**, 7195 (2014).
- [30] G. R. Lázaro, A. Hernández-Machado, and I. Pagonabarraga, *Soft Matter* **10**, 7207 (2014).
- [31] M. Fogliano, A. N. Morozov, O. Henrich, and D. Marenduzzo, *Phys. Rev. Lett.* **119**, 208002 (2017).
- [32] M. Fogliano, A. N. Morozov, and D. Marenduzzo, *Soft Matter* **14**, 9361 (2018).
- [33] L. Fei, A. Scagliarini, K. H. Luo, and S. Succi, *Soft Matter* **16**, 651 (2020).

- [34] R. Benzi, S. Chibbaro, and S. Succi, *Phys. Rev. Lett.* **102**, 026002 (2009).
- [35] See Supplemental Material at <http://link.aps.org/supplemental/10.1103/PhysRevE.107.035106> for further validation and the effect of system size and packing fraction.
- [36] Z. Guo, C. Zheng, and B. Shi, *Phys. Rev. E* **65**, 046308 (2002).
- [37] S. S. Chikatamarla and I. V. Karlin, *Phys. Rev. E* **79**, 046701 (2009).
- [38] T. Krüger, H. Kusumaatmaja, A. Kuzmin, O. Shardt, G. Silva, and E. M. Viggien, *The Lattice Boltzmann Method* (Springer, Cham, 2017).
- [39] R. Benzi, M. Sbragaglia, S. Succi, M. Bernaschi, and S. Chibbaro, *J. Chem. Phys.* **131**, 104903 (2009).
- [40] X. Shan, *Phys. Rev. E* **73**, 047701 (2006).
- [41] M. Sbragaglia, R. Benzi, L. Biferale, S. Succi, K. Sugiyama, and F. Toschi, *Phys. Rev. E* **75**, 026702 (2007).
- [42] A. Montessori, G. Falcucci, M. L. Rocca, S. Ansumali, and S. Succi, *J. Stat. Phys.* **161**, 1404 (2015).
- [43] G. Falcucci, G. Bella, G. Shiatti, S. Chibbaro, M. Sbragaglia, and S. Succi, *Commun. Comput. Phys.* **2**, 1071 (2007).
- [44] B. Dollet, A. Scagliarini, and M. Sbragaglia, *J. Fluid Mech.* **766**, 556 (2015).
- [45] G. Falcucci, S. Ubertini, C. Biscarini, S. D. Francesco, D. Chiappini, S. Palpacelli, A. D. Maio, and S. Succi, *Commun. Comput. Phys.* **9**, 269 (2011).
- [46] C. Peng, L. F. Ayala, O. M. Ayala, and L.-P. Wang, *Comput. Fluids* **191**, 104257 (2019).
- [47] R. C. V. Coelho, C. B. Moura, M. M. T. da Gama, and N. A. M. Araújo, *Int. J. Numer. Methods Fluids* **93**, 2570 (2021).
- [48] L. Lanotte, J. Mauer, S. Mendez, D. A. Fedosov, J.-M. Fromental, V. Claveria, F. Nicoud, G. Gompper, and M. Abkarian, *Proc. Natl. Acad. Sci. USA* **113**, 13289 (2016).
- [49] M. Kroupa, M. Soos, and J. Kosek, *Phys. Chem. Chem. Phys.* **19**, 5979 (2017).
- [50] C. D. Cwalina and N. J. Wagner, *J. Rheol.* **58**, 949 (2014).
- [51] A. Vananroye, P. Van Puyvelde, and P. Moldenaers, *J. Rheol.* **51**, 139 (2007).
- [52] A. Vananroye, P. J. A. Janssen, P. D. Anderson, P. Van Puyvelde, and P. Moldenaers, *Phys. Fluids* **20**, 013101 (2008).
- [53] H. Schlichting and K. Gersten, *Boundary-Layer Theory*, 9th ed. (Springer, Berlin, 2017), pp. 101–142.
- [54] A. Koponen, M. Kataja, and J. Timonen, *Phys. Rev. E* **56**, 3319 (1997).
- [55] A. Guariguata, M. A. Pascall, M. W. Gilmer, A. K. Sum, E. D. Sloan, C. A. Koh, and D. T. Wu, *Phys. Rev. E* **86**, 061311 (2012).
- [56] P. Sajeesh, M. Doble, and A. K. Sen, *Biomicrofluidics* **8**, 054112 (2014).
- [57] M. Sbragaglia, R. Benzi, M. Bernaschi, and S. Succi, *Soft Matter* **8**, 10773 (2012).
- [58] R. Benzi, M. Sbragaglia, A. Scagliarini, P. Perlekar, M. Bernaschi, S. Succi, and F. Toschi, *Soft Matter* **11**, 1271 (2015).
- [59] L. Fei, A. Scagliarini, A. Montessori, M. Lauricella, S. Succi, and K. H. Luo, *Phys. Rev. Fluids* **3**, 104304 (2018).